Estimating Land and Sea Surface Temperature From Cross-Calibrated Chinese Gaofen-5 Thermal Infrared Data Using Split-Window Algorithm

Xiangchen Meng, *Student Member, IEEE*, and Jie Cheng, *Member, IEEE*

***Abstract*— In this letter, the National Oceanic and Atmospheric Administration Joint Polar Satellite System enterprise algorithm and the quadratic split-window (SW) algorithm were adapted to high spatial resolution thermal infrared (TIR) data of Chinese Gaofen-5 (GF5) to estimate the land surface temperature (LST) and sea surface temperature (SST), respectively. Lacking official calibration coefficients, GF5 TIR data were cross-calibrated by the well-characterized Visible Infrared Imaging Radiometer Suite (VIIRS) data. The coefficients of two SW algorithms were obtained by linear regression from the simulated data set generated via comprehensive radiative transfer modeling. The performance of the two algorithms was first evaluated by independent simulation data and then cross-validated by Moderate Resolution Imaging Spectroradiometer (MODIS) LST/SST, VIIRS LST/SST, and Advanced Himawari Imager (AHI) SST products. The preliminary results show good agreement between estimated GF5 LSTs/SSTs and referenced LST/SST products, with an average bias (root mean square error) of −0.26 (1.74), −2.48 (3.49), 0.18 (2.43), and −1.47 K (2.86 K) for VLSTO, VNP21, MYD11, and MYD21 LST products, −0.79 (1.55), −0.28(1.58), and −1.71 (2.21) K for VIIRS, MODIS, and AHI SST products. This is the first time that both LST and SST are retrieved from the real GF5 data. This letter provides a practical method to estimate LST and SST from Chinese Gaofen-5.**

***Index Terms*— Cross-calibration, Gaofen-5 (GF5), land surface emissivity (LSE), land surface temperature (LST), sea surface temperature (SST).**

I. Introduction

SURFACE temperature including land surface temperature (LST) and sea surface temperature (SST) is one of the key parameters in the earth's surface energy and water budgets on local, regional, and global scales [1], [2], which has been used in many research fields such as evapotranspiration, weather forecast, and global climate change [3]–[7]. LSTs and SSTs obtained from satellite observations are of great potential benefit to a regional or global study. For example, Moderate Resolution Imaging Spectroradiometer (MODIS) and Advanced Very High Resolution Radiometer (AVHRR) LST products have been used for accessing forest fire risk [8], [9]. SST anomalies have been used to forecast El Niño and the Southern Oscillation (ENSO) [10].

Chinese Gaofen-5 (GF5) is the polar-orbiting satellite of the China High-resolution Earth Observation System (CHEOS) satellite [11], which was successfully launched on May 9, 2018. The orbit altitude is 705 km and local time of the ascending node is 13:30. Visual and infrared multispectral imager (VIMI) payload on the GF5 satellite has four thermal infrared (TIR) channels centered at 8.20 (band9: 8.01∼8.39 μm), 8.63 (band10: 8.42∼8.83 μm), 10.80 (band11: 10.30∼11.30 μm), and 11.95 μm (band12: 11.40∼12.50 μm). The TIR image has a spatial resolution of 40 m and the visible, near-infrared, and shortwave images have a spatial resolution of 20 m. GF-5 imagery has significant potential for exploring the urban ecological environment, water management, and natural disasters, by virtue of the high spatial resolution.

During the past two years, several algorithms, including split-window (SW) algorithm [11]–[14], temperature and emissivity separation (TES) algorithm [15], and hybrid algorithm [16], have been proposed to retrieve LST or SST from simulated GF5 TIR data. For example, Ye *et al.* [13] developed a four-channel SW algorithm to estimate LST from GF5 TIR data simulated from Thermal Airborne Spectrographic Imager (TASI) hyperspectral TIR data set. The root mean square errors (RMSEs) of GF5 LST are 0.45, 0.81, and 0.58 K, respectively, at three field sites. When GF5 TIR data simulated from Advanced Spaceborne Thermal Emission and Reflection Radiometer (ASTER) data were used, the hybrid algorithm can achieve an error of less than 1 K and 0.015 for LST and land surface emissivity (LSE). Nonlinear SW algorithms were used by Tang [11] for estimating LST and SST from simulated GF5 TIR data, and the preliminary evaluation results showed that the RMSE of LSTs (SSTs) is less than 0.7 K (0.3 K). Chen *et al.* [14] developed an SW algorithm to estimate SST from simulated GF5 TIR data, and the bias and RMSE are −0.05 and 0.53 K, respectively, when validated by *in situ* SST.

Although the accuracy of LST/SST retrieved from simulated GF5 TIR data is acceptable, the performance of these algorithms on real GF5 TIR data remains unknown, because many kinds of uncertainties during the data acquisition process

Manuscript received March 1, 2019; revised May 7, 2019; accepted June 4, 2019. This work was supported in part by the National Key Research and Development Program of China under Grant 2016YFA0600101, in part by the National Natural Science Foundation of China under Grant 41771365, and in part by the Civil Aerospace Technology Pre-Research Project of 13th Five-Year Plan under Grant 2017-S054. *(Corresponding author: Jie Cheng.)*

The authors are with the State Key Laboratory of Remote Sensing Science, Faculty of Geographical Science, Beijing Normal University, Beijing 100875, China, and also with the Institute of Remote Sensing Science and Engineering, Faculty of Geographical Science, Beijing Normal University, Beijing 100875, China (e-mail: Jie_Cheng@bnu.edu.cn).

Color versions of one or more of the figures in this letter are available online at http://ieeexplore.ieee.org.

Digital Object Identifier 10.1109/LGRS.2019.2921863

cannot be incorporated in the analog data through simple simulation, e.g., systematic error and random error. Regarding the GF5 data, two key issues are need to be solved to obtain operational LST/SST product. One is radiometric calibration, because the official calibration coefficients are unavailable so far. The other is a robust algorithm. Thus, the objective of this letter aims to develop a practical SW algorithm for GF5 to obtain LST/SST products. Sections II and III introduce SW algorithms and radiometric cross-calibration. Results and discussion are presented in Section IV. The conclusion is provided in Section V.

II. Methodology

A. Split-Window Algorithm

Meng *et al.* [17] demonstrated that the National Oceanic and Atmospheric Administration (NOAA) Joint Polar Satellite System (JPSS) enterprise algorithm has a comparable accuracy to the generalized SW (GSW) algorithm [18] and the SW algorithm designed by Sobrino *et al.* [19]. Thus, the NOAA JPSS enterprise algorithm was used to estimate LST from GF5 TIR data in this letter. According to the research of Yu *et al.* [20], the NOAA JPSS enterprise algorithm can be expressed as follows:

$$\mathrm{LST} = C_0 + C_1 T_{\mathrm{i}} + C_2(T_i - T_j) + C_3\varepsilon + C_4\varepsilon(T_i - T_j) + C_5\Delta\varepsilon \tag{1}$$

where T_i and T_j are the GF5 brightness temperatures of the channels i and j, respectively; $\varepsilon = (\varepsilon_i + \varepsilon_j)/2$ and $\Delta\varepsilon = \varepsilon_i - \varepsilon_j$ are the mean and difference of the channel emissivity, respectively. $C_i (i = 0{\sim}5)$ are the algorithm coefficients to be determined from simulated data.

B. Land Surface Emissivity Estimation

The LSE was determined from GF5 optical data [21]. Soil emissivity was estimated from the surface reflectance of GF5 visible and near-infrared channel [22], [23]. The emissivity of vegetated area was estimated by the vegetation cover method [24]. The formulas for calculating LSE are expressed as follows:

$$\varepsilon_i = \begin{cases} a_{1\ i} + \displaystyle\sum_{j=2}^{n} a_{ji}\rho_j & \mathrm{NDVI} < \mathrm{NDVIs} \\ \varepsilon_{vi} P_v + \varepsilon_{si}(1 - P_v) + 4\ d\varepsilon P_v (1 - P_v) & \mathrm{NDVIs} \le \mathrm{NDVI} \end{cases} \tag{2}$$

where ε_i is the LSE of two SW channels; ε_{vi} and ε_{si} are the vegetation and soil component emissivity, respectively; ρ_j is the surface reflectance of the visible, near-infrared band j, which was extracted from the imagery corrected by fast line-of-sight atmospheric analysis of spectral hypercubes (FLAASH); a_{ji} is the coefficient ($j = 1 \sim n$); P_v is the fractional vegetation cover; $\mathrm{NDVI}_s = 0.2$ and $\mathrm{NDVI}_v = 0.86$ are assigned [13]

$$P_v = \left[\frac{\mathrm{NDVI} - \mathrm{NDVI_s}}{\mathrm{NDVI}_v - \mathrm{NDVI}_s}\right]^2 \tag{3}$$

$d\varepsilon$ represents the emissivity increment from the cavity effect caused by the multiple scattering in the pixel, which can be expressed by [25], [26]

$$d\varepsilon = \begin{cases} \varepsilon_{vi}(-0.435\varepsilon_{si} + 0.4343)/0.985 & \varepsilon_{vi} \neq 0.985 \\ -0.435\varepsilon_{si} + 0.4343 & \varepsilon_{vi} = 0.985. \end{cases} \tag{4}$$

C. Sea Surface Temperature Algorithm

According to Coll *et al.* [27] and Niclòs *et al.* [28], considering the sea surface as a blackbody, the quadratic SW algorithm used to estimate SST can be expressed as follows:

$$\mathrm{SST} = C_0 + C_1(T_i - T_j) + C_2(T_i - T_j)^2 + T_i \tag{5}$$

where T_i and T_j are the GF5 brightness temperatures of the channels i and j, respectively; $C_i (i = 0{\sim}2)$ are the algorithm coefficients determined in the next part using the simulated data.

D. Simulation Data Set

The coefficients of two SW algorithms were obtained by linear regression using the simulated GF5 brightness temperatures generated by the SeeBor V5.0 global profiles (hereafter SeeBor) and MODTRAN 5.0. In total, 2762 (939) atmospheric profiles acquired on land (sea) surface under clear sky conditions are considered based on the research of Galve *et al.* [29]. For a realistic simulation using limited atmospheric profiles, the LSTs varies from T0 − 5 K to T0 + 20 K in steps of 5 K [17], [30] and the SSTs varies from T0 − 3 to T0 + 3 in steps of 3 K [28]. T0 is the bottom layer temperature of the SeeBor atmospheric profiles. For LSE simulation, 110 emissivity spectra from the ASTER and MODIS spectral library [31], [32] were selected, whereas five water emissivity spectra were selected for sea surface emissivity simulation. Finally, the algorithm coefficients in (1) and (5) are derived by a least-squares method.

E. Algorithm Coefficients

To improve the accuracy of the retrieved LST/SST, two SW algorithms were fit based on six water vapor content subranges: 0.0–2.5, 2.0–3.5, 3.0–4.5, 4.0–5.5, 5.0–7.0, and 0.0–7.0 cm. The algorithm coefficients and uncertainties of two SW algorithms are shown in Tables I and II. As shown in Table I, it is evident that the uncertainties of the estimated LST increase with the increase in water vapor content, and the RMSEs are all between 0.44 and 0.94 K under various water vapor contents. The estimated SST uncertainties also have a similar trend at the first four water vapor content subranges, and RMSEs range from 0.10 to 0.45 K. Under 5.0–7.0 and 0.0–7.0 cm subranges, the uncertainties of SST algorithm are 0.43 and 0.24 K.

III. Radiometric Cross-Calibration

The radiometric calibration of TIR data is a critical step toward generating high-level products. However, the official calibration coefficients are unavailable. In this letter, Visible Infrared Imaging Radiometer Suite (VIIRS) imagery was used for cross-calibration by following two reasons: first, VIIRS has similar thermal channels with GF5 and the spectral response functions are shown in Fig. 1.

TABLE I

COEFFICIENTS AND UNCERTAINTY OF THE LST ALGORITHM IN DIFFERENT WATER VAPOR CONTENT SUBRANGES

TWV(cm)	0.0-2.5	2.0-3.5	3.0-4.5	4.0-5.5	5.0-7.0	0.0-7.0
C0	50.52	51.90	40.65	14.96	-1.65	55.43
C1	1.02	1.00	1.00	1.01	1.00	1.00
C2	2.71	5.89	8.42	12.14	14.36	-6.09
C3	-55.17	-53.63	-41.30	-20.01	-1.97	-56.21
C4	-1.02	-3.52	-5.60	-8.92	-10.37	8.79
C5	-111.96	-101.72	-79.10	-55.41	-40.57	-121.8
RMSE(K)	0.44	0.53	0.64	0.79	0.94	0.92

TABLE II

COEFFICIENTS AND UNCERTAINTY OF THE SST ALGORITHM IN DIFFERENT WATER VAPOR CONTENT SUBRANGES

TWV(cm)	0.0-2.5	2.0-3.5	3.0-4.5	4.0-5.5	5.0-7.0	0.0-7.0
C0	0.06	-0.20	-0.71	-1.03	-2.23	0.11
C1	1.98	2.58	3.25	3.09	3.63	1.70
C2	0.01	-0.18	-0.27	-0.02	-0.02	0.33
RMSE(K)	0.10	0.24	0.38	0.45	0.43	0.24

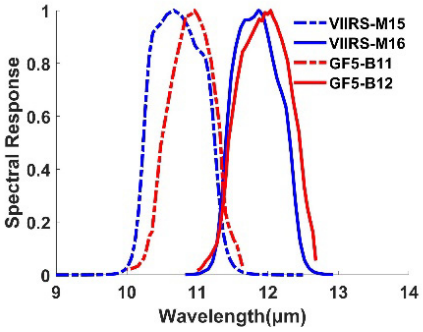

Fig. 1. Spectral response functions for GF5 and VIIRS.

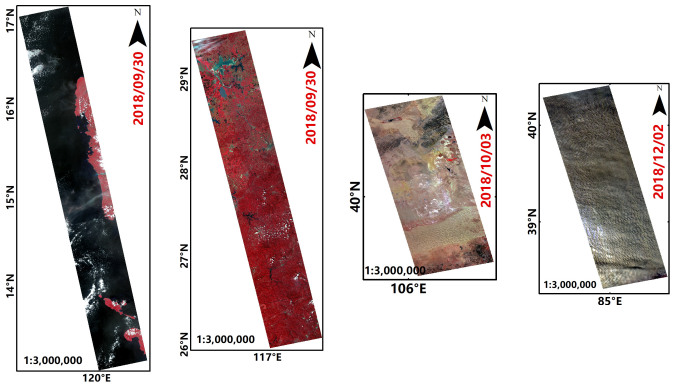

Fig. 2. Example of false-color images of Chinese GF5 data.

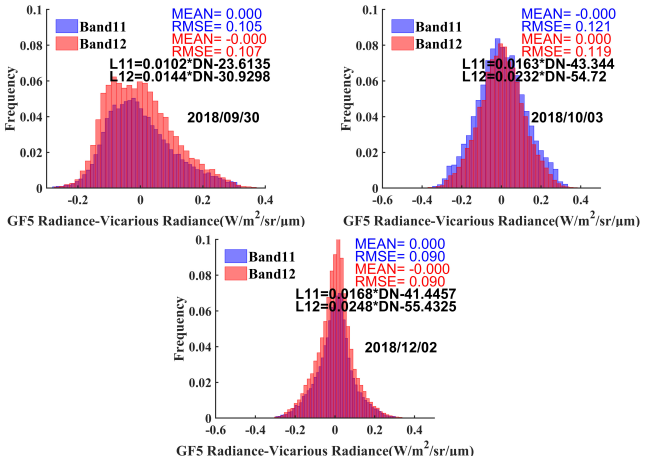

Fig. 3. Cross-calibration results for two TIR bands.

Second, previous works [33] demonstrated that the VIIRS has high calibration accuracy. The cross-calibration has three key steps: 1) calculate at-sensor radiances of GF5 at nadir view and VIIRS at various view zenith angles (VZAs) using the simulated data in Section II-D; 2) establish the relationship between at-sensor radiances of GF5 at nadir view and that of VIIRS at various VZAs; and 3) calculate the calibration coefficients with the at-sensor radiances and corresponding digital numbers (DNs) of GF5 image. Finally, the original GF5 TIR data can be calibrated to at-sensor radiances (L_i) by the following expression:

$$L_i = \text{Gain} * \text{DN} + \text{Offset}. \tag{6}$$

In theory, both GF5 and VIIRS pixels should be matched at nadir. However, we just get very limited matched imageries due to the narrow width and long revisit time of GF5, so GF5 pixels at nadir resampled using pixel aggregate method were matched with VIIRS pixels at various VZAs. Note the overpass time difference between GF5 and VIIRS is 35 min. In total, 22 scenes of the GF5 data were collected on September 30, 2018, October 03, 2018, and December 02, 2018. Currently, the GF5 TIR images are subjected to real-time onboard calibration, so the images of three dates are cross-calibrated separately. Water and sand have long been used as the primary target for vicarious calibration due to its spatial homogeneity and long-term stability [34], [35]. Imageries primarily covered by seawater and sand were used to obtain calibration coefficients. The mosaic images of Chinese GF5 data are shown in Fig. 2.

IV. RESULTS AND DISCUSSION

A. Radiometric Cross-Calibration Results

The cross-calibration results are shown in Fig. 3. The mean deviation and RMSE are about 0 (0) and 0.1 (0.1) W/m^2·sr·μm for Band 11 (Band 12). The radiance difference between calibrated GF5 radiance and vicarious radiance ranged from -0.373 (-0.36) to 0.359 (0.446) W/m^2 · sr · μm for Band 11 (Band 12). Assuming the brightness temperature of Band 11 and Band 12 to be 300 K, the brightness temperature variation caused by the above radiance uncertainty ranged from 297.39 (297.03) to 302.45 K (303.59 K) for Band 11 (Band 12). So far, the calibration coefficients are not stable, which means real-time calibration is required.

B. Algorithm Testing With Independent Profiles

A total of 4714 (3610) Global Atmospheric Profiles from Reanalysis Information (GAPRI) profiles [36] over land (sea) surface were choose to test the performance of two SW algorithms. Fig. 4. shows the biases and RMSEs of two SW algorithms when evaluated by GAPRI profiles. Under various

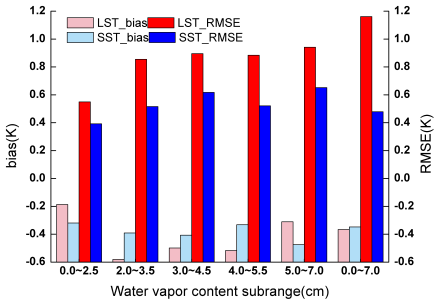

Fig. 4. Bias and RMSE of two SW algorithms when evaluated by GAPRI profiles.

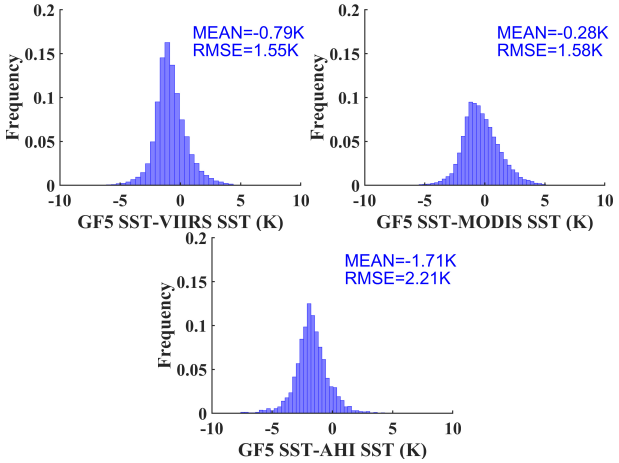

Fig. 5. Cross-validation result of estimated GF5 SST on September 30, 2018.

water vapor content subranges, the RMSEs of SST are all less than that of LST. The RMSEs are 0.55 (0.39), 0.86 (0.52), 0.90 (0.62), 0.88 (0.52), 0.94 (0.65), and 1.16 K (0.48 K) for LST (SST), whereas those values are −0.19 (−0.32), −0.58 (−0.39), −0.50 (−0.41), −0.52 (−0.33), −0.31 (−0.48), and −0.37 K (−0.35 K) for biases, respectively.

C. Preliminary Validation and Discussion

The coefficients of SW algorithms are selected based on the MODIS Water Vapor data product (MYD05_L2). The cloud mask for GF5 data was obtained from the supervised classification of GF5 visible and near-infrared images. Ideally, *in situ* LSTs collected from homogeneous surfaces should be used to conduct validation. Unfortunately, such data are unavailable in this letter. Thus, the retrieved GF5 LST/SST was validated by MODIS LST/SST, VIIRS LST/SST, and Advanced Himawari Imager (AHI) SST products. The products derived from SW algorithm (MYD11_L2, VLSTO) and TES algorithm (MYD21, VNP21) were used for validation. The overpass time differences between GF5 and other TIR sensors are less than 30 min. The pixel aggregate method was used to match the GF-5 pixels to other TIR sensors pixels during LST/SST cross-validation. The validation results of GF5 LST and SST are shown in Fig. 5 and Table III. Note that MODIS image on December 2, 2018, is covered by cloud, so there are no data in Table III.

When validated by MYD11, the biases of enterprise algorithm on September 30, 2018, and October 3, 2018,

TABLE III
CROSS-VALIDATION RESULT OF GF5 LST ESTIMATED FROM ENTERPRISE ALGORITHM

		MYD11	MYD21	VLSTO	VNP21
09/30	bias(K)	1.55	-0.47	0.53	-0.16
	RMSE(K)	2.59	2.49	2.18	2.56
10/03	bias(K)	-1.2	-2.46	-1.09	-3.64
	RMSE(K)	2.27	3.22	1.99	4.08
12/02	bias(K)	-	-	-0.21	-3.64
	RMSE(K)	-	-	1.05	3.84
Mean bias(K)		0.18	-1.47	-0.26	-2.48
Mean RMSE(K)		2.43	2.86	1.74	3.49

were 1.55 and −1.2 K, respectively, whereas the values when validated by MYD21 were −0.47 and −2.46 K, respectively. When validated by VIIRS LST, the biases of enterprise algorithm on September 30, 2018, October 3, 2018, and December 2, 2018, were 0.53, −1.09, and −0.21 K, respectively, whereas the values when validated by VNP21 were −0.16, −3.64, and −3.64 K, respectively. The RMSEs of enterprise algorithm between GF5 LST and four LST products for three dates were between 1.05 and 4.08 K. When VIIRS, MODIS, and AHI SSTs were used for validation, the biases of the quadratic SW algorithm were −0.79, −0.28, and −1.71 K, respectively. The RMSEs of quadratic SW algorithm between GF5 SST and three SST products were 1.55, 1.58, and 2.21 K, respectively. The preliminary validation results demonstrate that both LST and SST estimated from the SW algorithm can achieve comparable accuracy with MODIS and VIIRS products.

We found that the retrieved LSTs over bare soil are lower than MODIS and VIIRS LST products. One reason may explain this result. The LSEs are obtained from optical data without rigorous radiometric calibration, which may introduce large uncertainties in the estimated LSE. Taking ASTER global emissivity database as a reference, we found that retrieved LSEs of two bands are overestimated on average to about 0.019 and 0.01 for Bands 11 and 12, which may result in an underestimation of the LST.

The effect of cloud contamination may explain the large uncertainties in the estimated SST. Although most of the clouds can be identified from the supervised classification, the thin cloud is not well recognized. Moreover, some phenomena existing in GF5 TIR images, such as noticeable striping and banding, are worth mentioning. This requires more processing to improve the quality of the GF5 image before quantitative inversion. The above two reasons may introduce large deviations into the retrieved SST. In addition, more GF5 data need to be collected for comprehensive analysis.

V. CONCLUSION

In this letter, the NOAA JPSS enterprise algorithm and the quadratic SW algorithm were adapted to retrieve LST/SST from high spatial resolution TIR data of Chinese GF5. As the

official calibration coefficients are unavailable, GF5 TIR data was cross-calibrated by VIIRS imagery before surface temperature retrieval. A new land surface scheme was used to determine the LSE of GF5. The coefficients of two SW algorithms were derived using simulated data generated from the SeeBor profiles and ASTER/MODIS emissivity spectra. Simulated data sets derived from GAPRI profiles were used to test the performance of two SW algorithms. The biases (RMSEs) of the enterprise algorithm were between −0.58 (0.55) and −0.19 K (1.16 K), and the biases (RMSEs) of the quadratic SW algorithm were between −0.48 (0.39) and −0.32 K (0.65 K). When VIIRS and MODIS LST products were used for validation, the average biases (RMSEs) ranged from −2.48 (1.74) to 0.18 (3.49) K, whereas those values ranged from −1.71 (1.55) to −0.28 (2.21) K when VIIRS, MODIS, and AHI SST are used for validation. The preliminary validation results indicate that both LST and SST estimated from SW algorithm can achieve acceptable accuracy.

This is the first time that both LST and SST are retrieved from the real GF5 data. This letter will improve the application level of GF5 data and benefit the research fields that need high spatial resolution surface temperature.

ACKNOWLEDGMENT

The GF5 data used were provided by the Ministry of Ecology and Environment Center for Satellite Application on Ecology and Environment.

REFERENCES

[1] A. Karnieli *et al.*, "Use of NDVI and land surface temperature for drought assessment: Merits and limitations," *J. Climate*, vol. 23, pp. 618–633, Feb. 2010.

[2] J. Hsiung, "Mean surface-energy fluxes over the global ocean," *J. Geophys. Res.-Oceans*, vol. 91, no. 9, pp. 585–606, Sep. 1986.

[3] E. Valor and V. Caselles, "Mapping land surface emissivity from NDVI: Application to European, African, and South American areas," *Remote Sens. Environ.*, vol. 57, no. 3, pp. 167–184, 1996.

[4] J. Cheng, S. Liang, J. Wang, and X. Li, "A stepwise refining algorithm of temperature and emissivity separation for hyperspectral thermal infrared data," *IEEE Trans. Geosci. Remote Sens.*, vol. 48, no. 3, pp. 1588–1597, Mar. 2010.

[5] J. Hansen, R. Ruedy, M. Sato, and K. Lo, "Global surface temperature change," *Rev. Geophys.*, vol. 48, no. 4, p. 1, Dec. 2010.

[6] X. Meng, J. Cheng, and S. Liang, "Estimating land surface temperature from Feng Yun-3C/MERSI data using a new land surface emissivity scheme," *Remote Sens.*, vol. 9, no. 12, p. 1247, Dec. 2017.

[7] X. Meng and J. Cheng, "Evaluating eight global reanalysis products for atmospheric correction of thermal infrared sensor—Application to Landsat 8 TIRS10 Data," *Remote Sens.*, vol. 10, p. 474, Mar. 2018.

[8] L. Manzo-Delgado, S. Sánchez-Colón, and R. Álvarez, "Assessment of seasonal forest fire risk using NOAA-AVHRR: A case study in central Mexico," *Int. J. Remote Sens.*, vol. 30, no. 19, pp. 4991–5013, Sep. 2009.

[9] G. Guo and M. Zhou, "Using MODIS land surface temperature to evaluate forest fire risk of northeast China," *IEEE Geosci. Remote Sens. Lett.*, vol. 1, no. 2, pp. 98–100, Apr. 2004.

[10] S. A. Klein, B. J. Soden, and N. C. Lau, "Remote sea surface temperature variations during ENSO: Evidence for a tropical atmospheric bridge," *J. Climate*, vol. 12, pp. 917–932, Apr. 1999.

[11] B.-H. Tang, "Nonlinear split-window algorithms for estimating land and sea surface temperatures from simulated Chinese Gaofen-5 satellite data," *IEEE Trans. Geosci. Remote Sens.*, vol. 56, no. 11, pp. 6280–6289, Nov. 2018.

[12] Y. Chen, S.-B. Duan, H. Ren, J. Labed, and Z.-L. Li, "Algorithm development for land surface temperature retrieval: Application to Chinese Gaofen-5 data," *Remote Sens.*, vol. 9, p. 161, Feb. 2017.

[13] X. Ye, H. Ren, R. Liu, Q. Qin, Y. Liu, and J. Dong, "Land surface temperature estimate from Chinese Gaofen-5 satellite data using split-window algorithm," *IEEE Trans. Geosci. Remote Sens.*, vol. 55, no. 10, pp. 5877–5888, Oct. 2017.

[14] Y. Chen, S.-B. Duan, J. Labed, and Z.-L. Li, "Development of a split-window algorithm for estimating sea surface temperature from the Chinese Gaofen-5 data," *Int. J. Remote Sens.*, vol. 40, pp. 1621–1639, Aug. 2018.

[15] Y. Yang *et al.*, "A temperature and emissivity separation algortihm for Chinese gaofen-5 satelltie data," in *Proc. IEEE Int. Geosci. Remote Sens. Symp. (IGARSS)*, Jul. 2018, pp. 2543–2546.

[16] H. Ren, X. Ye, R. Liu, J. Dong, and Q. Qin, "Improving land surface temperature and emissivity retrieval from the Chinese gaofen-5 satellite using a hybrid algorithm," *IEEE Trans. Geosci. Remote Sens.*, vol. 56, no. 2, pp. 1080–1090, Feb. 2018.

[17] X. Meng, J. Cheng, S. Zhao, S. Liu, and Y. Yao, "Estimating land surface temperature from Landsat-8 data using the NOAA JPSS enterprise algorithm," *Remote Sens.*, vol. 11, p. 155, Jan. 2019.

[18] Z. Wan and J. Dozier, "A generalized split-window algorithm for retrieving land-surface temperature from space," *IEEE Trans. Geosci. Remote Sens.*, vol. 34, no. 4, pp. 892–905, Jul. 1996.

[19] J. A. Sobrino *et al.*, "Multi-channel and multi-angle algorithms for estimating sea and land surface temperature with ATSR data," *Int. J. Remote Sens.*, vol. 17, no. 11, pp. 2089–2114, 1996.

[20] Y. Yu, Y. Liu, P. Yu, and H. Wang, "Enterprise algorithm theoretical basis document for VIIRS land surface temperature production," p. 22, Oct. 2017.

[21] J. Cheng, S. Liang, A. Nie, and Q. Liu, "Is there a physical linkage between surface emissive and reflective variables over non-vegetated surfaces?" *J. Indian Soc. Remote Sens.*, vol. 46, no. 4, pp. 591–596, 2018.

[22] B.-H. Tang *et al.*, "An improved NDVI-based threshold method for estimating land surface emissivity using MODIS satellite data," *Int. J. Remote Sens.*, vol. 36, nos. 19–20, pp. 4864–4878, 2015.

[23] J. Cheng and S. Liang, "Estimating the broadband longwave emissivity of global bare soil from the MODIS shortwave albedo product," *J. Geophys. Res., Atmos.*, vol. 119, no. 2, pp. 614–634, Jan. 2014.

[24] E. Valor, V. Caselles, and S. G. Pandalai, "Validation of the vegetation cover method for land surface emissivity estimation," in *Proc. Recent Res. Develop. Thermal Remote Sens.*, Kerala, India, 2005, pp. 1–20.

[25] J. Cheng, S. Liang, W. Verhoef, L. Shi, and Q. Liu, "Estimating the hemispherical broadband longwave emissivity of global vegetated surfaces using a radiative transfer model," *IEEE Trans. Geosci. Remote Sens.*, vol. 54, no. 2, pp. 905–917, Feb. 2016.

[26] E. Valor and V. Caselles, "Validation of the vegetation cover method for land surface emissivity estimation," in *Recent Research Developments in Thermal Remote Sensing*, V. Caselles, E. Valor, and C. Coll, Eds. Kerala, India: Res. Signpost, 2005, pp. 1–20.

[27] C. Coll, V. Caselles, J. A. Sobrino, and E. Valor, "On the atmospheric dependence of the split-window equation for land surface temperature," *Int. J. Remote Sens.*, vol. 15, no. 1, pp. 105–122, 1994.

[28] R. Niclòs, V. Caselles, C. Coll, and E. Valor, "Determination of sea surface temperature at large observation angles using an angular and emissivity-dependent split-window equation," *Remote Sens. Environ.*, vol. 111, pp. 107–121, Nov. 2007.

[29] J. M. Galve, C. Coll, V. Caselles, and E. Valor, "An atmospheric radiosounding database for generating land surface temperature algorithms," *IEEE Trans. Geosci. Remote Sens.*, vol. 46, no. 5, pp. 1547–1557, May 2008.

[30] J.-C. Jimenez-Munoz and J. A. Sobrino, "Split-window coefficients for land surface temperature retrieval from low-resolution thermal infrared sensors," *IEEE Geosci. Remote Sens. Lett.*, vol. 5, no. 4, pp. 806–809, Oct. 2008.

[31] A. M. Baldridge, S. J. Hook, C. I. Grove, and G. Rivera, "The ASTER spectral library version 2.0," *Remote Sens. Environ.*, vol. 113, no. 4, pp. 711–715, 2009.

[32] W. C. Snyder, Z. Wan, Y. Zhang, and Y.-Z. Feng, "Thermal Infrared (3–14 μm) bidirectional reflectance measurements of sands and soils," *Remote Sens. Environ.*, vol. 60, no. 1, pp. 101–109, 1997.

[33] X. Xiong *et al.*, "VIIRS on-orbit calibration methodology and performance," *J. Geophys. Res., Atmos.*, vol. 119, no. 9, pp. 5065–5078, 2014.

[34] J. A. Barsi, J. R. Schott, S. J. Hook, N. J. Raqueno, B. L. Markham, and R. G. Radocinski, "Landsat-8 thermal infrared sensor (TIRS) vicarious radiometric calibration," *Remote Sens.*, vol. 6, no. 11, pp. 11607–11626, 2014.

[35] B. Zhong, Y. Zhang, T. Du, A. Yang, W. Lv, and Q. Liu, "Cross-calibration of HJ-1/CCD over a desert site using landsat ETM + imagery and ASTER GDEM product," *IEEE Trans. Geosci. Remote Sens.*, vol. 52, no. 11, pp. 7247–7263, Nov. 2014.

[36] C. Mattar, C. Durán-Alarcón, J. C. Jiménez-Muñoz, A. Santamaría-Artigas, L. Olivera-Guerra, and J. A. Sobrino, "Global atmospheric profiles from reanalysis information (GAPRI): A new database for earth surface temperature retrieval," *Int. J. Remote Sens.*, vol. 36, nos. 19–20, pp. 5045–5060, 2015.